Proceedings of TURBO EXPO Turbine Technical Conference and Exposition
TURBO EXPO 2011
June 6-10, 2011, Vancouver, Canada

GT2010-45906

INVESTIGATION OF CALCULATED TURBULENCE PARAMETERS FOR USE IN HYBRID BROADBAND FAN NOISE CALCULATIONS

Jeremy Maunus
Sheryl M. Grace
Department of Mechanical Engineering
Boston University
Boston, MA 02215
Email: jrmaunus@bu.edu

Douglas L. Sondak
Scientific Computing
and Visualization
Boston University
Boston, MA 02215
Email: sondak@bu.edu

Victor Yakhot
Department of Mechanical Engineering
Boston University
Boston, MA 02215
Email: vy@bu.edu

ABSTRACT

The ability to predict the broadband noise due to fluid-structure interaction in the fan-stage of a turbofan engine could enhance engine design. Currently, fully computational hybrid schemes for coupling RANS flow simulations and linearized Euler acoustic simulations offer a potential broadband noise prediction methodology. The success of the hybrid method depends partly on the ability of RANS to accurately predict the turbulent kinetic energy and the integral length scale. The impact of the accuracy of a RANS simulation on the broadband noise prediction is explored. NASAs Source Diagnostic Test (SDT), a 1/5th scale model representation of the bypass stage of a turbofan engine provides the basis for the computations and validations. The RSI (rotor-stator interaction) code is utilized to compute the fan exit guide vane response and exhaust noise due to the interaction with inflow turbulence. The experimental data for the baseline vane SDT case at the approach condition are analyzed using structure functions to obtain the turbulent kinetic energy, dissipation rate, and integral length scale. These results are compared to the solutions provided by four proprietary CFD codes that employ two-equation turbulence models. The CFD simulations are shown to predict the turbulent kinetic energy well, over-predict mean dissipation rate, and capture the integral length scale moderately well. The broadband exhaust noise computed with RSI based on input derived from the various CFD simulations differ and it is shown that the differences are most strongly dependent upon the variation in the estimation of the integral length scale.

NOMENCLATURE

- k mean turbulent kinetic energy per unit mass
- r separation distance
- S_n^s nth order streamwise (longitudinal) structure function
- S_n^t nth order transverse structure function
- S_n^u nth order upwash structure function
- $\mathbf{u}(\mathbf{x},t)$ total velocity vector
- $\mathbf{u}'(\mathbf{x},t)$ turbulent velocity vector
- $\mathbf{U}(\mathbf{x},t)$ time-dependent mean velocity vector
- $\mathbf{x}$ position vector
- ε mean energy dissipation rate per unit mass
- Λ_i integral length scale in the i^{th} direction
- ν kinematic viscosity
- τ separation time

Introduction

Computational methods for the prediction of broadband interaction noise generated by the fan-stage of a turbofan engine hinges upon reasonable prediction of the fan-wake turbulence. The methods currently being developed for broadband fan interaction noise are two step methods. In the first step, the wake turbulence is defined either from experiment or from computation. Then, the interaction of the wake turbulence with the vane is computed using a linearized Euler based simulation. In most cases, the vane simulation provides the vane's unsteady aerodynamic response as well as the resulting acoustics in the annular duct downstream of the vane. The feasiblity of full computa-

tional prediction, in which both steps rely on computation, motivates the present research.

Due to computational costs, rotating machinery computations rely on Reynolds Averaged Navier Stokes (RANS) computational fluid dynamic (CFD) simulations. Turbulence is represented in RANS through the turbulence model. Often two-equation models such as $k-\varepsilon$ and $k-\omega$ are used. In these models, the turbulent kinetic energy is defined by $k = \overline{u_i' u_i'}/2$ and the mean dissipation rate by $\varepsilon = \nu \overline{\frac{\partial u_i'}{\partial x_j} \frac{\partial u_i'}{\partial x_j}}$, where u' is the *turbulent* component of the velocity field.

In the current investigation, four RANS simulations of the source diagnostic test (SDT) fan-stage test rig at approach condition are compared and validated. Experimental hot-wire measurements at two locations in the gap between the fan rotor and the fan exit guide vane (FEGV) provide the basis for the validation. The determination of the turbulent kinetic energy from the experimental data is straight forward. The mean dissipation rate is computed from the experimental data using structure functions. The relationship between ε and the 2nd order structure function is based on the exact fluid dynamical definition of the dissipation rate in statistically isotropic flow and it allows one to compute ε without knowledge of the spectrum.

The prediction of the broadband interaction noise is carried out using the RSI code distributed by NASA [1]. Inputs for the RSI code include the passagewise distribution of the turbulent kinetic energy just upstream of the fan exit guide vane (FEGV) and the integral length scale of the turbulence at radial locations hub-to-tip. A method for estimating the integral length scale from the RANS turbulence parameters is described. It is then shown that the prediction of the length scale varies widely across the four RANS simulations. Finally, it is shown that differences in the predicted noise for the SDT approach case when the input is taken from the four different RANS simulations or the experimental data are linked strongly to the differences in the predicted integral length scale.

1 Source Diagnostic Test

A primary goal of the Source Diagnostic Test (SDT), a 1999-2000 study conducted in the 9'x15' Low Speed Wind Tunnel at NASA Glenn, was to better understand and reduce fan interaction noise. The SDT utilized a 1/5 scale fan stage and bypass duct based on a General Electric turbofan engine [2]. The flow in the gap between the fan and FEGV was measured at two locations: HW1 (2.96 inches) and HW2 (5.89 inches) referenced to the static position of the fan tip trailing edge. A side-view of the fan-stage is shown in figure 1 [2]. Laser Doppler Velocimetry (LDV) data were obtained for several operating conditions at two axial locations. At the lower wheel speeds hot-wire anemometer data were also obtained. The hot-wire probes used were 4-wire, 3-component systems outfitted with 5μm diameter tungsten wires.

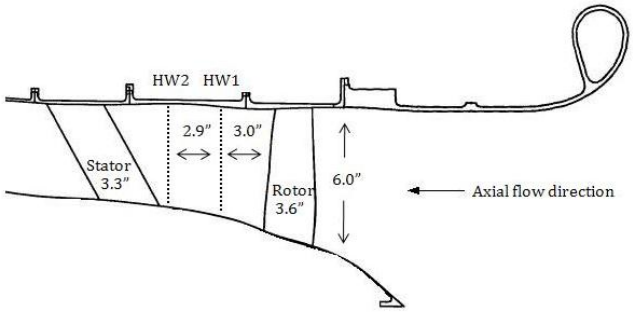

FIGURE 1. Schematic of SDT Rig (side-view)

The measurements from these dual cross-wire probes are of particular interest to this study, as many properties of the turbulent field can be deduced from the acquired velocity time-traces. Data were obtained at 50 radial positions. The hotwire data were obtained for the 22-blade R4 rotor running at 7,808 rpm (approach condition) with an FEGV configuration of 26-vanes swept at 30° (low-noise case). The design stage pressure ratio for the fan is 1.47. At the pitchline the rotor blade chord is 3.61 inches while the vane chord is 3.26 inches. Two other FEGV configurations were tested. The case with 54 unswept vanes (baseline case) is used for the noise simulations in this work.

2 Computational solutions

The solutions from four proprietary RANS CFD simulations with embedded two-equation turbulence models that had been used to simulate the SDT approach condition baseline vane case were obtained. The features of the RANS CFD simulations include:

CFD1 utilizes a version of the Wilcox $k-\omega$ turbulence model and is loosely coupled in that it simulates both the fan and the FEGV but uses a one-on-one model and handles the mismatch in blade passages via special boundary conditions. CFD1 uses O and H meshes including a tip clearance region of 0.02 inches. The grid density between the upstream (HW1) and downstream (HW2) measurement stations is 95 (axial) by 36 (radial) by 64 (circumferential) points.

CFD2 uses a $k-\omega$ turbulence model and is also loosely coupled. CFD2 employs both C and H type grids and includes a tip clearance region of 0.04 inches. This simulation uses 86 (axial) by 81 (radial) by 89 (circumferential) grid points between the HW1 and HW2 axial stations.

CFD3 employs a $k-\varepsilon$ turbulence model and utilizes the average passage method for turbomachinery flows. This simu-

lation uses two H-grids, one in the rotor (relative) frame of reference and one in the stator (absolute) frame. The CFD3 simulation does not model the tip gap and uses 19 (axial) by 51 by 51 grid points between the two measurement locations.

CFD4 is a rotor-alone simulation which employs a $k-\omega$ turbulence model. This simulation uses both O and H type grids, and for the approach condition includes a tip clearance region of 0.02 inches and uses 53 (axial) by 113 (radial) by 49 (circumferential) grid points between the two hot-wire measurement positions.

The experimental measurements were made with a rubstrip installed in the SDT rig which was designed to provide a 0.02 inch clearance between the blade tip and the outer casing with the fan operating at 100% speed [2]. Also, CFD1, CFD2, and CFD3 simulate the flow field for the 54 unswept vane FEGV configuration, while the hot-wire data were acquired with the 26 swept vane low-noise stator installed. It has been assumed that for the approach condition, the potential effect of the nearby vanes on the flow field at the downstream hot-wire station is not strong.

A comparison of the mean flow prediction from the four CFD simulations has made previously [3, 4]. The previous study focused on the impact of variations in the predicted mean wakes on computational tonal noise predictions. The streamwise component of the centerspan average passage mean flow at the second hot-wire location is show in Figure 2. The circumferentially averaged velocity has been removed and the wakes have been centered for this comparison.

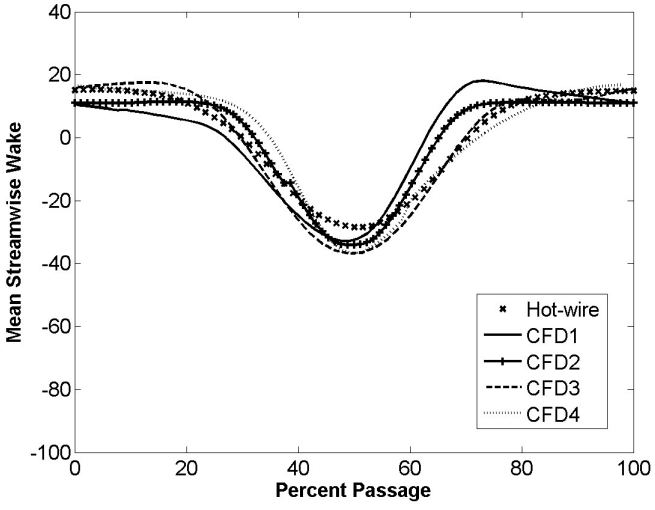

FIGURE 2. Average passage streamwise mean velocities (ft/s)

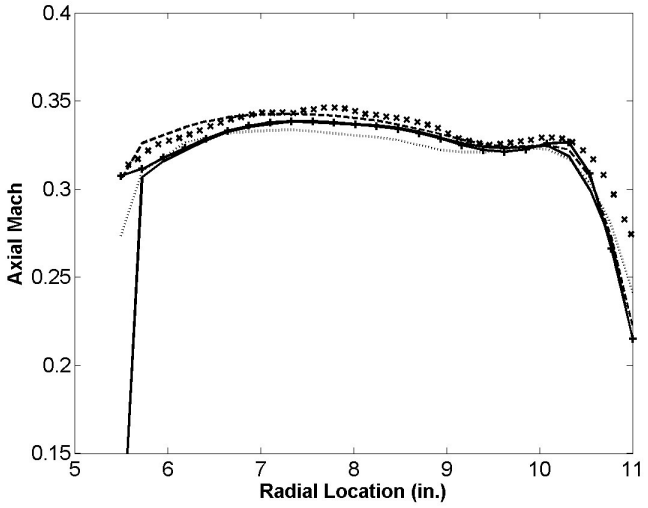

(a) Axial Mean

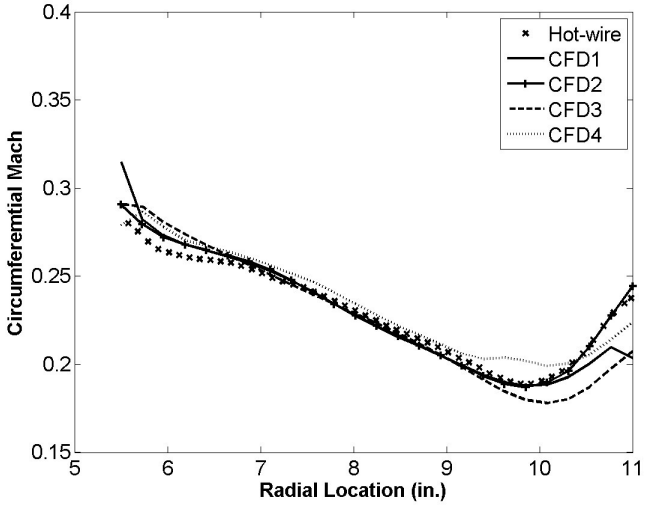

(b) Circumferential Mean

FIGURE 3. Radial distribution of mean flow (ft/s)

The radial distribution of the average axial and circumferential mean flows are shown in Figure 3. The agreement between the simulations and to data is remarkable. The largest differences are seen near the tip. However, the differences do not follow a trend with tip gap model. In fact, the results are remarkably similar near the tip given that the simulations cover a wide range of tip gap values.

3 Experimental Determination of the Turbulence Parameters

3.1 Turbulent Kinetic Energy

The hot-wire velocity measurements taken behind a rotor have strong periodic unsteadiness related to the blade passing frequency and its harmonics. Consequently, this deterministic unsteadiness must be removed from the signal to isolate the turbulent velocity fluctuations. As such, the velocity vector at a given location in such a system can be decomposed into a turbulent component and a time-dependent mean:

$$\mathbf{u}(t) = \mathbf{U}(t) + \mathbf{u}'(t) \tag{1}$$

The time dependent mean is obtained by averaging the data per passage location. The turbulent part of the signal is obtained then by removing the average passage velocity from the original velocity vector. The total mean kinetic energy per unit mass associated with the turbulent portion of the flow is then calculated using

$$k = \frac{1}{2}(\overline{u_1'^2} + \overline{u_2'^2} + \overline{u_3'^2}) \tag{2}$$

where the three directions correspond to u_1 : streamwise, u_2 : radial or transverse, and u_3 : upwash. The value of k is computed and then the average passage distribution of k is found. Figure 4, below, shows the turbulent kinetic energy field at both axial hot-wire stations. The average passage value has been repeated 22 times in the figure. Generally, the magnitude of k increases from hub to tip at each axial station and decreases from the upstream station to the downstream station. The turbulent kinetic energy become more diffuse downstream. Additionally, the spanwise phase distribution becomes more pronounced downstream because of the swirling flow.

Figure 5 displays the root-mean-square turbulent velocities in three directions for a passage at the midspan. Figure 6 shows the radial distributions of the circumferentially-averaged single-point correlations. For isotropic turbulence, the single-point correlations satisfy the following relations:

$$\overline{u_1'^2} = \overline{u_2'^2} = \overline{u_3'^2} \tag{3}$$

and

$$\overline{u_1'u_2'} = \overline{u_1'u_3'} = \overline{u_2'u_3'} = 0 \tag{4}$$

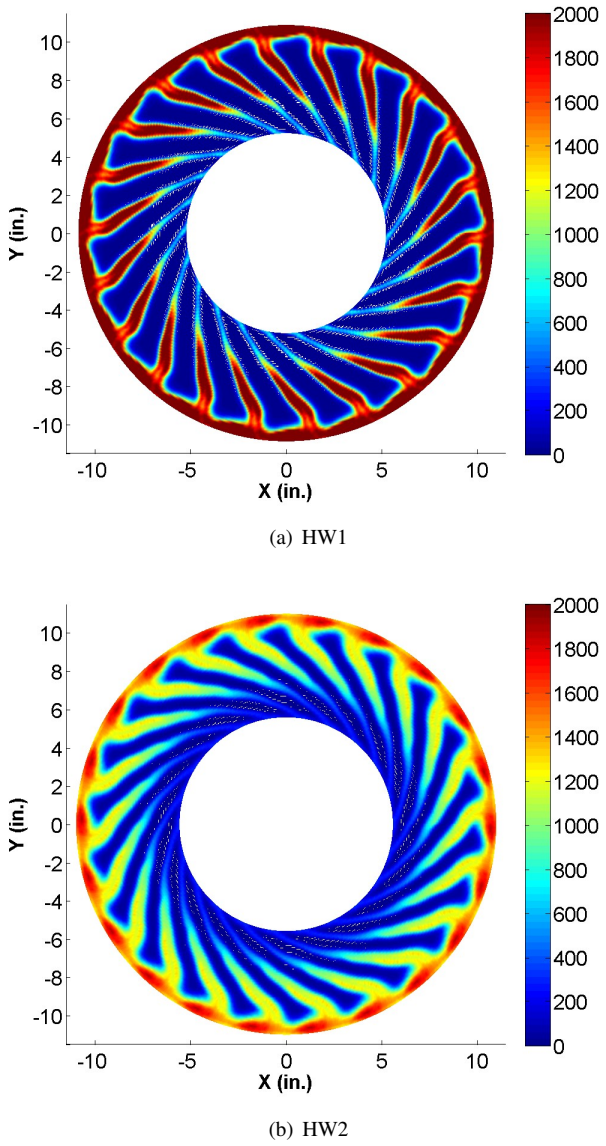

(a) HW1

(b) HW2

FIGURE 4. Average passage turbulent kinetic energy (ft^2/s^2)

Figure 6 confirms that the flow is least isotropic near the outer duct wall, in the vicinity of the tip-vortex, and in general it becomes more isotropic as it is convected farther from the rotor [2]. The flow near the inner duct wall at HW2 is slightly less isotropic than at the corresponding HW1 locations. This is potentially due to the proximity of the swept stators which are located just downstream of the HW2 inner radii measurement locations. Another difference of note between the upstream and downstream stations is the relative decrease in the magnitude of the upwash turbulent velocity from HW1 to HW2; this implies a change in the orientation of turbulent kinetic energy vector as the

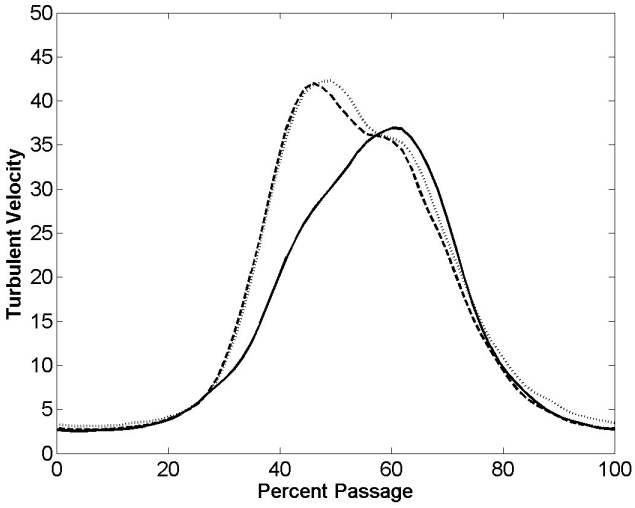

(a) HW1

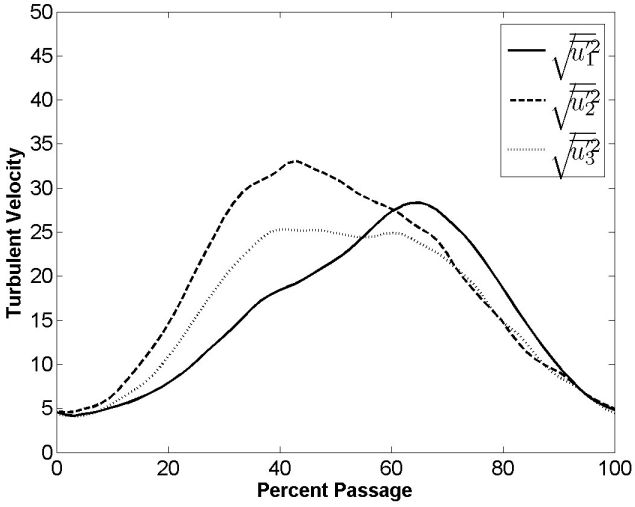

(b) HW2

FIGURE 5. Midspan passagewise mean square velocities (ft/s)

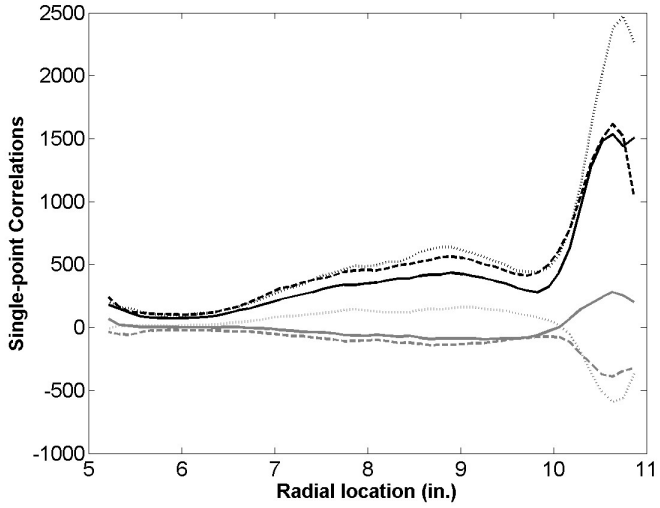

(a) HW1

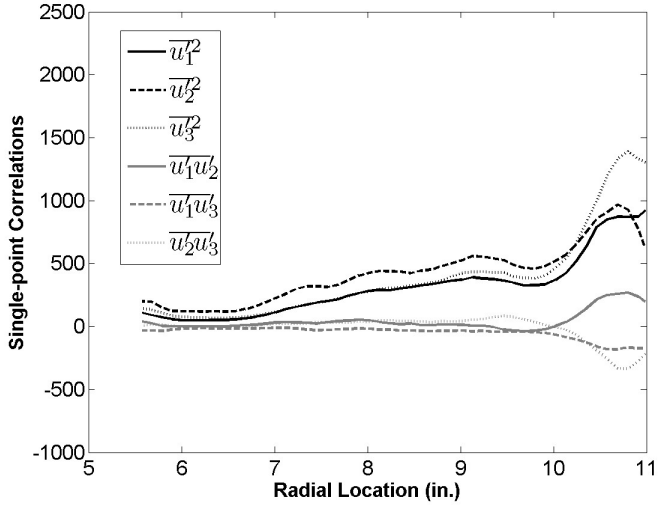

(b) HW2

FIGURE 6. Radial distribution of mean square velocities (ft^2/s^2)

turbulence is transported by the swirling annulus flow.

3.2 Dissipation Rate

The nth order velocity increment moments, or structure functions, are defined by

$$S_n = \overline{(\delta_r \mathbf{u}')^n} = \overline{\left((\mathbf{u}'(\mathbf{x}+\mathbf{r}) - \mathbf{u}'(\mathbf{x})) \cdot \frac{\mathbf{r}}{r}\right)^n}. \qquad (5)$$

Consider the second-order longitudinal (streamwise) structure functions, S_2^s. For homogeneous, isotropic turbulence, $S_2^s(r)$, is a function only of r, the separation distance, and follows a 2/3 power law in the inertial range. Taylor's frozen turbulence hypothesis, which is valid for $u'_{rms}/U_1 << 1$, assumes that the convection of a field of turbulence can be taken to be entirely due to the mean flow, giving $r = U_1\tau$. From Taylor's hypothesis, $S_2^s(r) = S_2^s(U_1\tau)$. And by definition:

$$\frac{\partial u_1}{\partial x_1} = \lim_{r\to 0} \frac{u_1(\mathbf{x}+\mathbf{r}\cdot\mathbf{i}) - u_1(\mathbf{x})}{r} = \lim_{\tau\to 0} \frac{u_1(\mathbf{x}+U_1\tau) - u_1(\mathbf{x})}{U_1\tau}, \tag{6}$$

where $\mathbf{i}$ is the unit vector in the streamwise direction. It is clear that for derivatives to be accurately evaluated the contributions on the order $O(r^2)$ must be negligibly small. This means that

$$\overline{\left(\frac{\partial u_1'}{\partial x_1}\right)^2} \approx \frac{S_2^s(r)}{r^2} \approx \frac{S_2^s(U_1\tau)}{(U_1\tau)^2} \tag{7}$$

evaluated in the analytic range of scales where $S_2^s(r) = \overline{\left(\frac{\partial u_1'}{\partial x_1}\right)^2} r^2$. Figure 7 shows the second-order structure functions in the three coordinate directions, computed at the midspan radial locations of both HW1 and HW2. For small separation times, at both hot-wire stations, the lateral (transverse and upwash) structure functions are approximately equal to twice the longitudinal structure functions.

The mean energy dissipation rate of locally isotropic turbulence is defined by [5, 6]

$$\varepsilon = 15\nu\overline{\left(\frac{\partial u_1'}{\partial x_1}\right)^2}, \tag{8}$$

where ν is the kinematic viscosity. Thus from Equation (7) the mean energy dissipation rate is obtained as

$$\varepsilon = \lim_{\tau\to 0} 15\nu \frac{S_2^s(U_1\tau)}{U_1^2\tau^2}. \tag{9}$$

That is, the turbulent kinetic energy dissipation rate can be directly calculated so long as the unsteady velocity measurements are taken with a short enough time-step such that for small r, $S_2(r)/r^2 \approx constant$. As seen in Figure 7, a slope of 2 is approached at the sampling time of the hot-wire probes which indicates that Equation (9) is appropriate for calculating the mean energy dissipation rate. For locally isotropic turbulence, ε can also be computed from the *lateral* second-order structure functions S_2^t and S_2^u via [5, 6]

$$\varepsilon = \frac{15}{2}\nu\overline{\left(\frac{\partial u_2'}{\partial x_1}\right)^2} = \lim_{\tau\to 0} \frac{15}{2}\nu \frac{S_2^t(U_1\tau)}{U_1^2\tau^2} = \lim_{\tau\to 0} \frac{15}{2}\nu \frac{S_2^u(U_1\tau)}{U_1^2\tau^2}. \tag{10}$$

Figure 8, shows the HW1 and HW2 midspan passagewise distributions of ε computed with Equations (9) and (10). Note

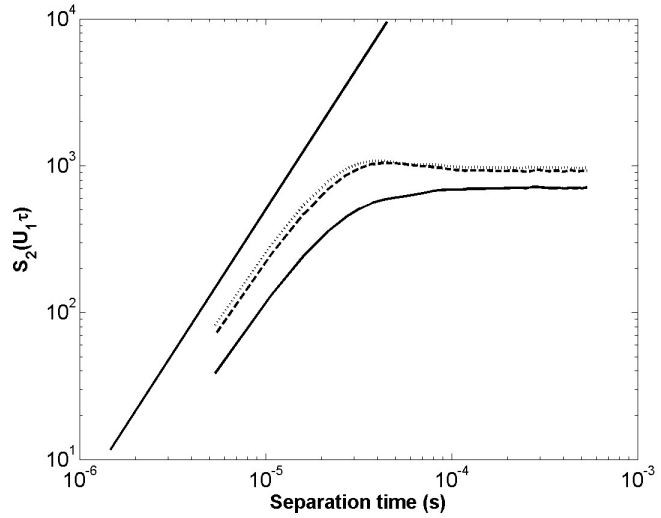

(a) HW1

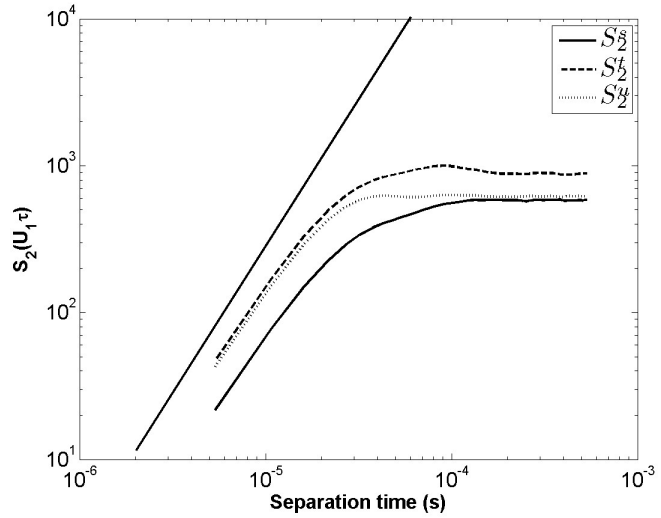

(b) HW2

FIGURE 7. Midspan second-order structure functions (ft^2/s^2)

that the time step used for these calculations is 5.37 μs, which corresponds to a hot-wire sampling rate of approximately 186 kHz. Also, the kinematic viscosity has been assumed to be a constant, namely 1.6412 x10^{-4} ft^2/s. Figure 8 reveals that the maximum mean dissipation rate is significantly larger at the HW1 midspan location compared to the HW2 midspan maximum and that the passagewise distribution is broader at HW2. This is as expected due to sharper turbulent velocity gradients present in the deeper, narrower upstream mean wakes. Further comparison of Figure 8(a) to 8(b) shows an increase in isotropy at the dissipation scale away from the rotor. Brasseur and Ye-

ung have shown by analysis of the Navier-Stokes equations in Fourier space that "in a turbulent flow the coupling between the large and the small scales persists and is dynamically significant in the infinite-Reynolds-number limit. Hence, anisotropy of the small scales can be induced by the anisotropy of the large scales. In fact, a finite level of small-scale anisotropy must always exist if the large scales are anisotropic." [7] Thus, given that the flow is more anisotropic at HW1, it is not surprising that the anisotropy in ε is more pronounced at HW1 as well.

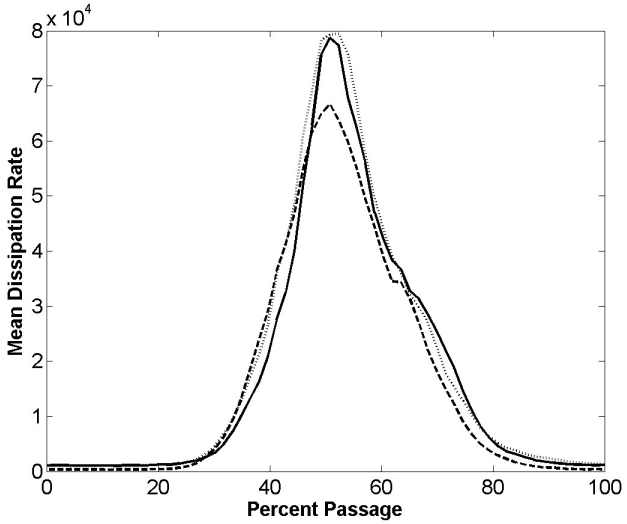

(a) HW1

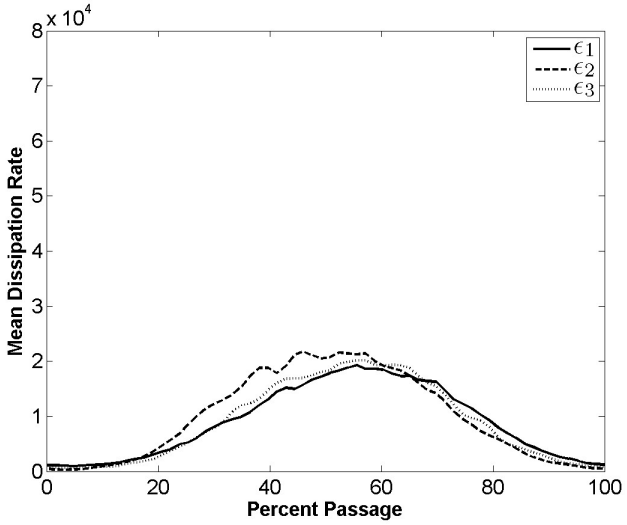

(b) HW2

FIGURE 8. Midspan passagewise mean dissipation rate (ft^2/s^3)

Figure 9 displays the radial distributions of the circumferentially-averaged mean dissipation rates, which were determined using Eq. (9) for the streamwise direction and Eq. (10) for the other two directions with the arithmetic mean streamwise velocity and the second-order structure functions computed using the entire filtered velocity time traces ($\sim$ 170,000 data points per measurement location). As expected, small-scale anisotropy is observed to be greatest near the tip regions of both axial stations. Also, despite the fact that the maximum ε values are nearly four times larger at the midspan HW1 radial location compared to a similar position at HW2, the circumferentially-averaged mean dissipation rates are only two times larger at HW1 due to the significantly broader passagewise distributions at HW2.

The turbulent kinetic energy of the flow can also be determined from the second-order structure functions because it is clear that in the limit of large time scales, for which the turbulent velocity correlation approaches zero, $S_2(U_1\tau)$ tends to a constant value of $2\overline{u_i'^2}$. Computing turbulent velocities using the second-order structure functions produces results nearly identical to those shown in Figures 5 and 6.

3.3 Length Scales

Previous studies have computed turbulent length scales within compressors [8] and turbine ducts [9] by way of integration of the autocorrelation coefficient. These authors use

$$\Lambda_i = \frac{\overline{U_1}}{\overline{u_i'^2}} \int_0^\infty u_i'(\tau) u_i'(\tau + t)\, dt. \tag{11}$$

Podboy [2] used this method to calculate the HW1 and HW2 radial distributions of the integral length scales for the SDT fan at the approach condition. Our analysis of the data shown in Figure 10 below reproduces his results . The downstream length scales are generally longer than their upstream counterparts since the wakes thicken as they are convected downstream. These length scales also increase from hub to tip at each axial station. The ratios of the streamwise length scale to each of the cross-stream length scales at a given radial position are on the order of 2. For isotropic turbulence, these ratios will be exactly 2; as discussed above, large-scale anisotropy exists to some extent at each of the 100 measurement points in this flow.

It is impossible to calculate passagewise distributions of the integral length scales with the available SDT data using the methods outlined above. Consequently, alternative techniques must be employed to determine the passagewise distribution of the streamwise integral length scale fields. Using phenomenology and simple scaling arguments [10], the streamwise length scale can be written in terms of the root-mean-square velocity (in the streamwise direction) and the mean dissipation rate, as

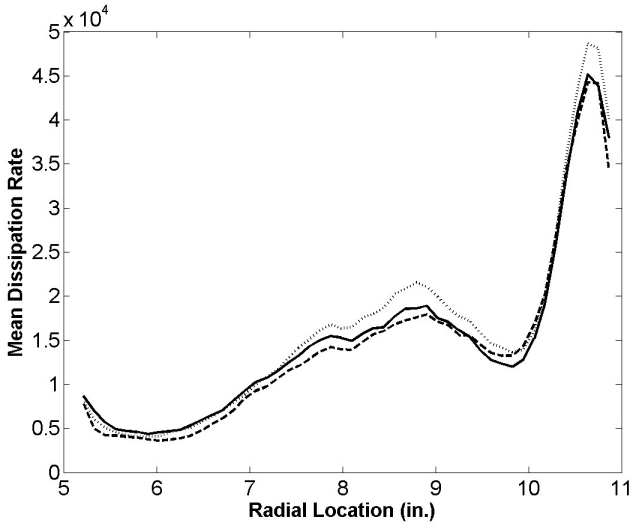

(a) HW1

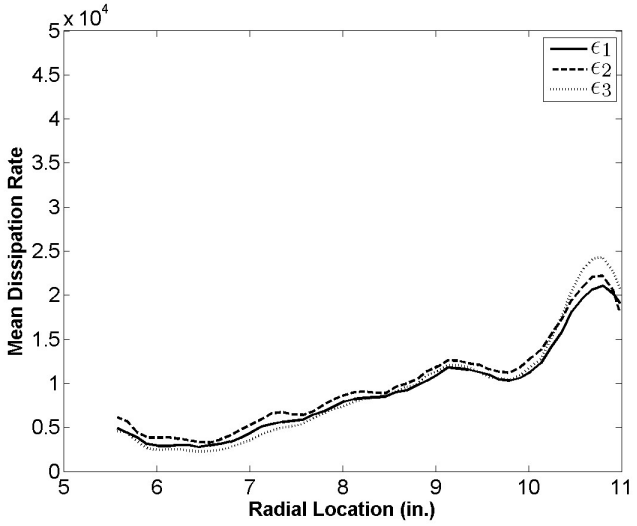

(b) HW2

FIGURE 9. Radial distribution of mean dissipation rate (ft^2/s^3)

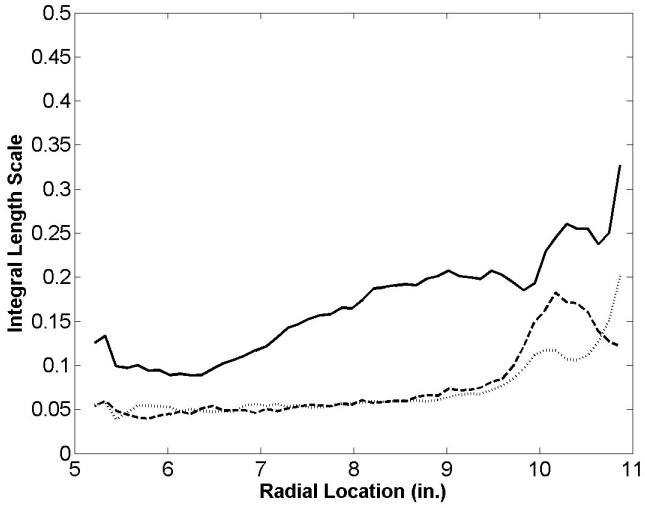

(a) HW1

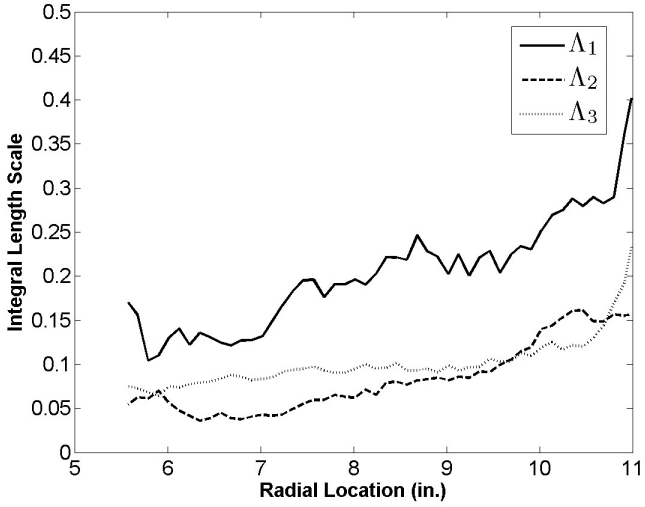

(b) HW2

FIGURE 10. Radial distribution of circumferentially averaged integral length scale (*inches*)

$$\Lambda_1 = C_\varepsilon \frac{u_{rms}'^3}{\varepsilon}. \tag{12}$$

As described by Donzis, Sreenivasan, and Yeung [11], the dissipation rate of turbulent energy is independent of the fluid viscosity in the limit of large Reynolds number. This has the consequence that C_ε asymptotically approaches a constant in the limit of high Reynolds numbers. Doering and Foias [12] supply the following functional form

$$C_\varepsilon = f(Re_\lambda) = A(1+\sqrt{1+(B/Re_\lambda)^2}), \tag{13}$$

where Re_λ is the Reynolds number based on the Taylor microscale, λ. In the streamwise direction the Taylor microscale is expressed by

$$\lambda_1^2 = \overline{u_1'^2} / \overline{\left(\frac{\partial u_1'}{\partial x_1}\right)^2} = \frac{15\nu\overline{u_1'^2}}{\varepsilon}, \tag{14}$$

Figure 11(a), below, shows the Reynolds-number dependence of C_ε. These data have been fit with curves in the manner of Seoud and Vassilicos [13], namely with C/Re_λ, where C is a constant, as well as with Eq. (13). The fits of the data are $25/Re_\lambda$ (dashed line) and $0.005(1+\sqrt{1+(4500/Re_\lambda)^2})$ (solid line). Donzis, Sreenivasan, and Yeung note that while the asymptotic dependence of C_ε shown in Figure 11(a) is universal for all types turbulent flows away from solid walls, it must be emphasized that "the coefficients A and B are not universal, even if one fixes the operational definitions of Λ_1 and u_1'. They depend on the type of flow, and, for a given flow, on detailed initial conditions." [11]

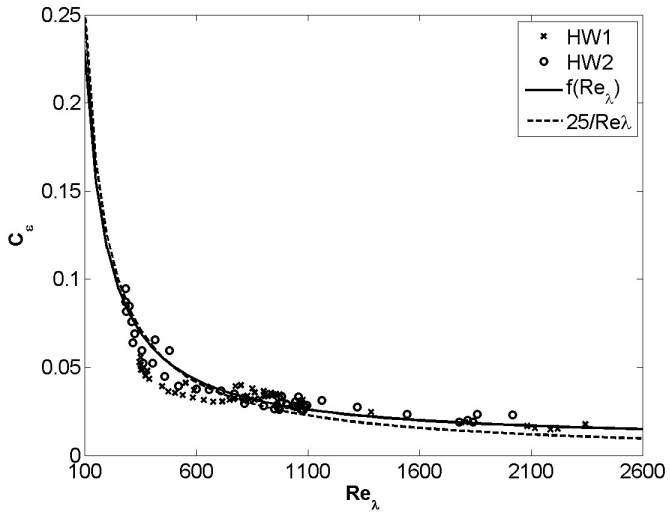

(a) C_ε versus Re_λ

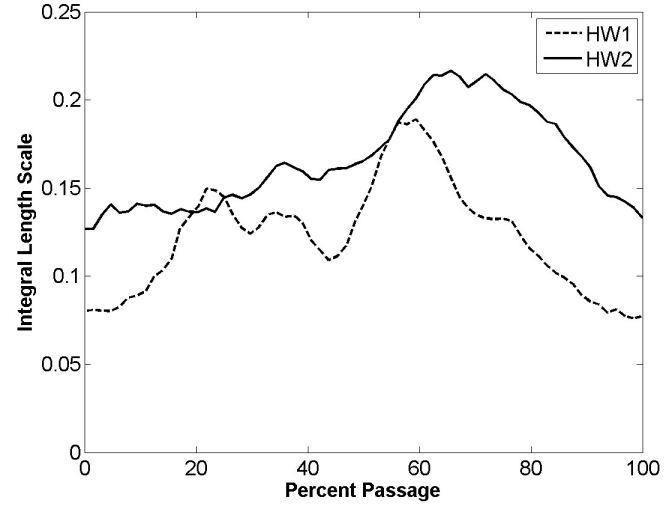

(b) Midspan Λ_1 (*in.*)

FIGURE 11. Calculation of C_ε and passagewise distribution of Λ_1

Subsequently, the passagewise streamwise integral length scales can be computed using Equations (12) and (14) with the appropriate constants. Figure 11(b) shows a passagewise plot of the HW1 and HW2 streamwise integral length scales at the midspan radial locations calculated using the $25/Re_\lambda$ relation. As with the circumferentially-averaged integral length scale (Figure 10), the passagewise distribution of Λ_1 is generally larger downstream than upstream. As the turbulence is convected away from the rotor, the passagewise distribution of the length scale becomes smoother as the mean wakes become thicker and more diffuse.

4 Computational Results

The results from the four simulations can be compared to the experimentally determined values of k, ε and Λ. The passage distribution of k at the center span is shown in Figure 12. The agreement between the computations themselves and the experimental value is quite reasonable. One feature that is important for the broadband calculation is the lower limit of k. It seems that the different simulations have imposed different limiting values for k.

The circumferentially averaged value of k is compared from hub to tip and shown in Figure 13. The CFD simulations provide fairly accurate predictions of the total mean turbulent kinetic energy at both hot-wire axial stations. Near the hub, CFD4 which is the rotor-alone simulation, gives k values which are twice those reported experimentally. However, for all radial positions outside of the hub region (approximately 7" to 11") CFD4 actually gives the best agreement with the experimental results. This reconciles with the fact that the experimental data are obtained with a swept vane configuration in which the leading edge of the vane is near the HW2 at the hub and farther from the HW2 at the tip. The simulations which include the downstream stator all model the straight vane and as such the leading edge of the vane is near the HW2 location from hub to tip in three of the simulations.

The passagewise distribution of ε predicted by CFD is shown in Figure 14. The dependent variables (k and ε or ω) are often limited in 2-equation models, and it appears that limiters are affecting some of the distributions in Fig. 14. Here the effect of limiters on ε is strong and the limiting values are very different across simulations. Also, the CFD solutions are shown to greatly overpredict the peak value of ε in the passage when compared to the experimentally determined value. This overprediction though is later shown to be consistent (and inconsequential) with the method for defining the length scale in the turbulence model.

The circumferentially averaged value of ε shown in Figure 15 from hub to tip demonstrates that the simulations predict the radial trend in ε fairly well and again are shown to be 50 times larger than the experimental values.

In order to compare the length scales, one must define a

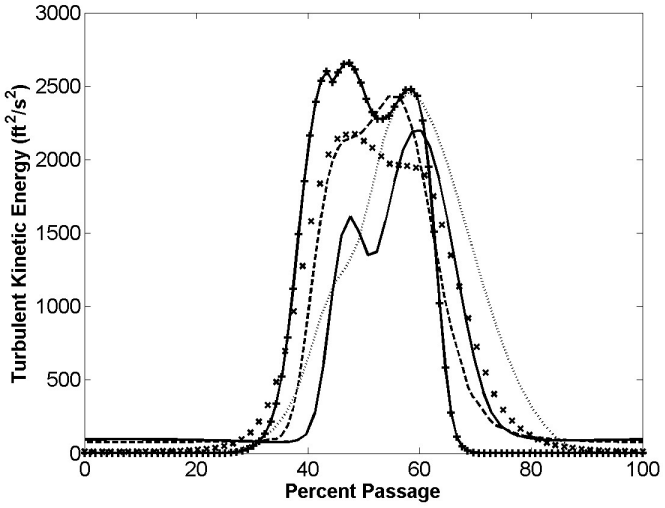

(a) HW1

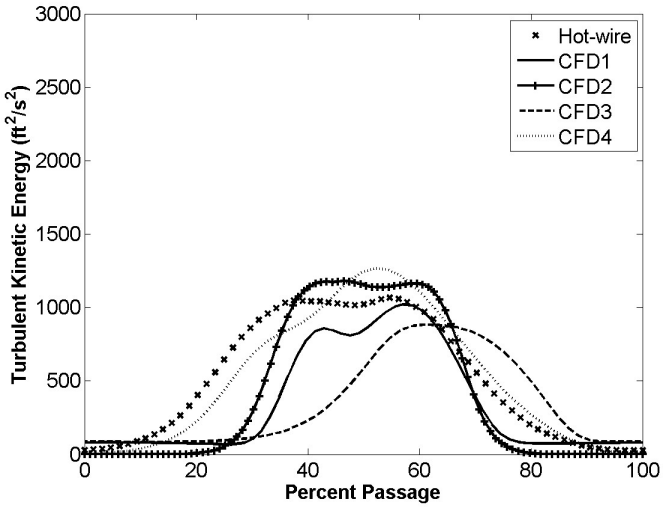

(b) HW2

FIGURE 12. Passagewise distribution of turbulent kinetic energy (ft^2/s^2).

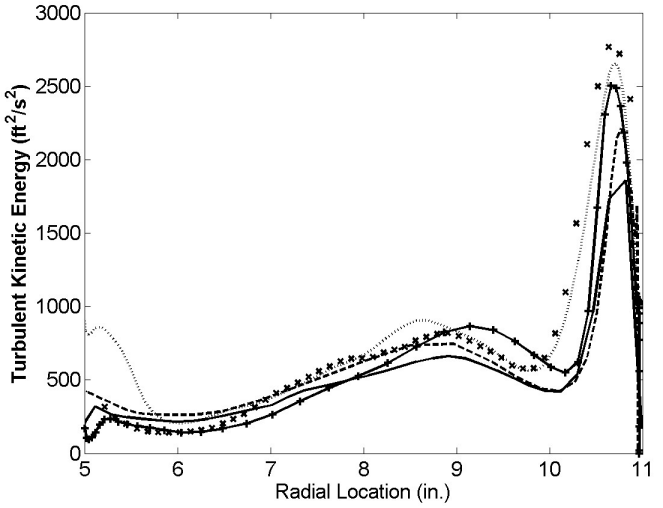

(a) HW1

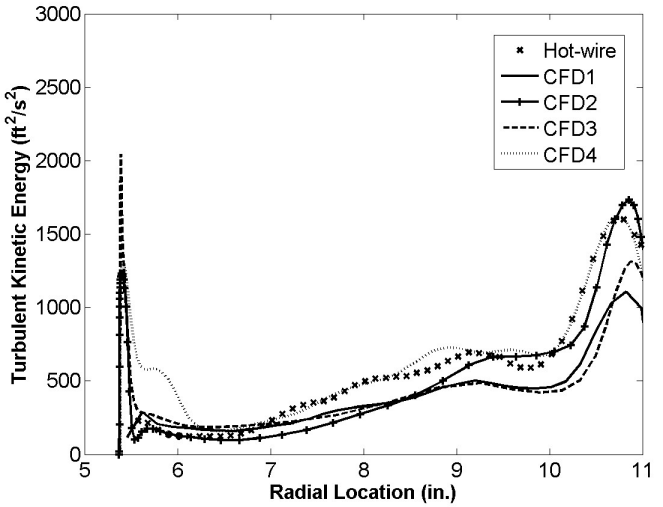

(b) HW2

FIGURE 13. Radial distribution of turbulent kinetic energy (ft^2/s^2).

method for obtaining the length scale from the CFD turbulence parameters. In the paper by Nallasamy and Envia [14] they note that when one computes $k^{3/2}/\varepsilon$ it is on the order of the integral length scale computed from the hot-wire data. This relation is related to Equation (12), however C_ε has arbitrarily been set to 1.0. When one uses this method to compute a length scale from the CFD results, the results are on the order of the experimentally determined integral length scale. Figure 16 shows the passagewise distribution of the length scale.

CFD1 gives a length scale about twice that based on experimental data at both hot-wire stations near the center span, CFD4 is very far off, and CFD2 gives the best overall agreement at HW2 (the location which is of greatest importance for broadband noise prediction). The radial distribution of the circumferentially averaged integral length scale is shown in shown in Figure 17. The length scale determined via the autocorrelation based on Eq. (11) (crosses) is shown as well as the length scale found based on Eq. (12) (circles). Three of the simulations agree well with each other while CFD4 gives results that are inaccurate near the hub and tip. CFD1, CFD2, and CFD3 all underpredict the experimentally based length scale value in the 50-90% span region. Nearer the hub, CFD2 underpredicts and CFD1 and CFD3 overpredict

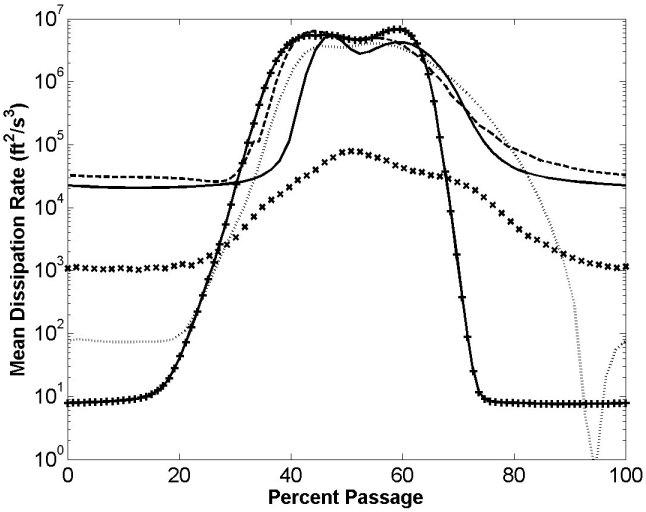

(a) HW1

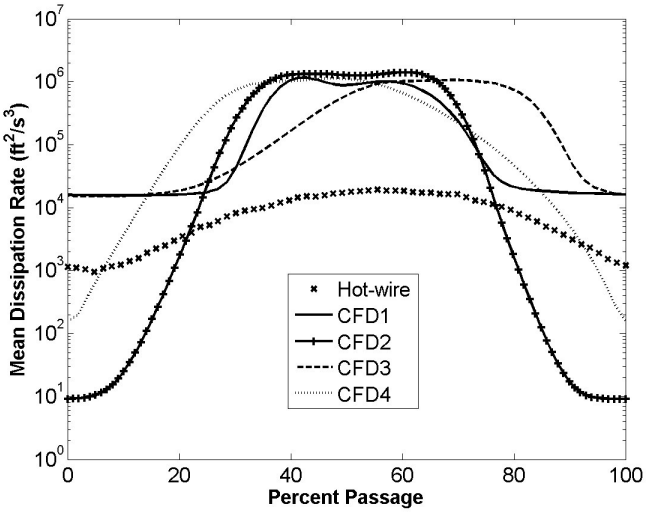

(b) HW2

FIGURE 14. Passagewise distribution of dissipation rate (ft^2/s^3).

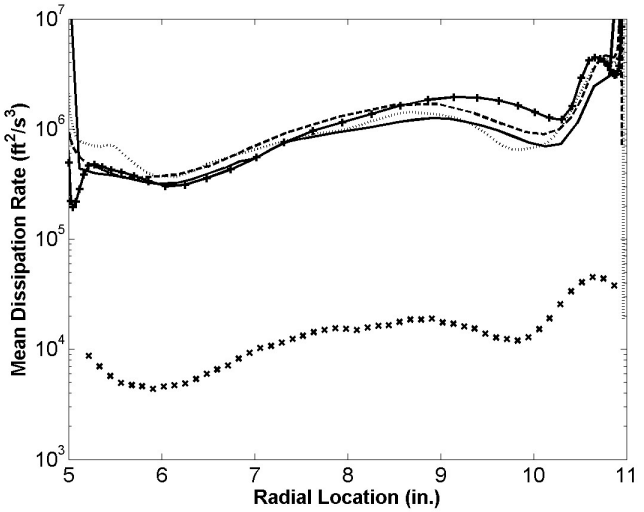

(a) HW1

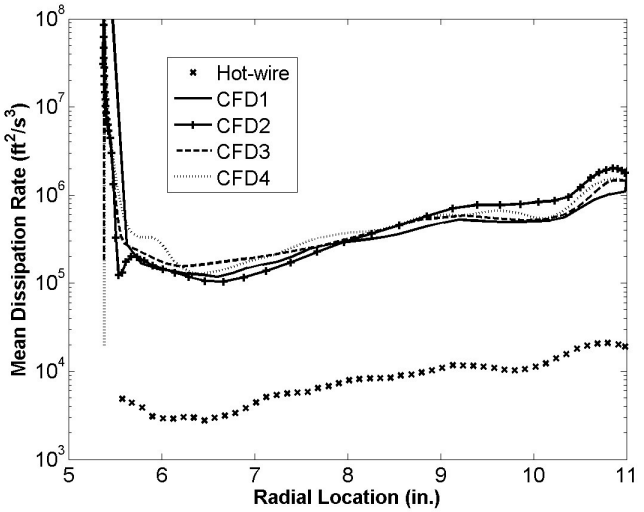

(b) HW2

FIGURE 15. Radial distribution of mean dissipation rate (ft^2/s^3).

the integral length scale determined via the structure functions. The differences are on the order of a factor of 2. Nearer the hub, the structure function method and the autocorrelation method for determining the length scale from the experimental data do not agree to within a factor of 2 either.

5 Impact on Broadband Noise Prediction

The broadband noise produced by a vane interacting with a given inflow turbulent field can be estimated using the NASA distributed RSI (rotor-stator interaction) code. This vane response code relies on a semianalytical two-dimensional flat-plate cascade response calculation in the frequency-wave number domain [15]. Strip theory is used to account for three-dimensional effects. The duct acoustics are predicted via the Green's function method in which the Green's function for an infinite cylindrical annulus is specified. Previous computations of broadband fan interaction noise with RSI are available in the literature. [1, 14] Field microphones were used in the SDT and a method for isolating the rotor-alone noise was used successfully at the lower wheel speeds. [16] The interaction noise contribution to the downstream duct power was calculated in the experiment then by subtracting the rotor-alone noise from the total sound

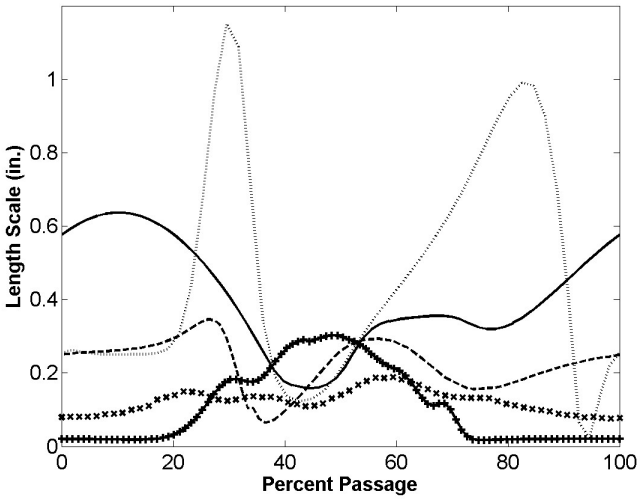

(a) HW1

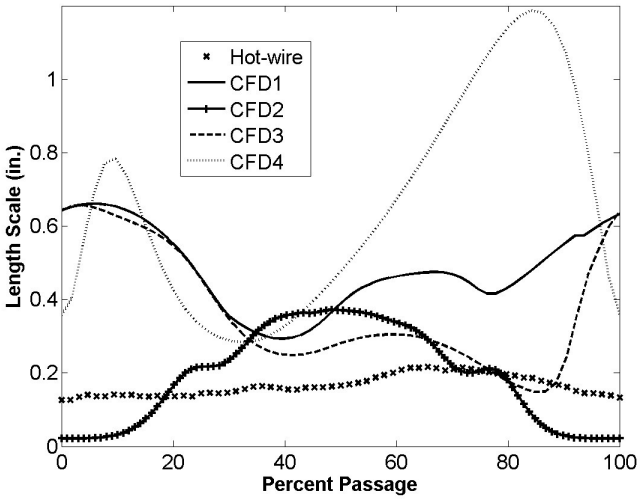

(b) HW2

FIGURE 16. Passagewise distribution of length scale.

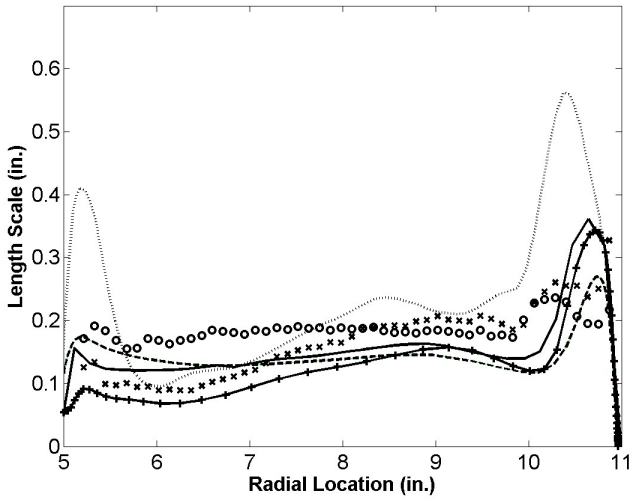

(a) HW1

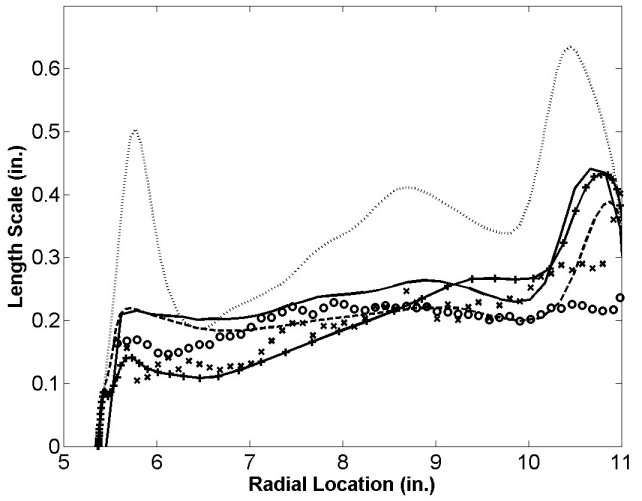

(b) HW2

FIGURE 17. Radial distribution of length scale. Experimental data: crosses -Eq. (11), circles - Eq. (12)

field.

RSI uses the passage distribution of the turbulent kinetic energy together with a spectral model of the turbulence at each radial location. The spectral model is based on Gaussian correlations and is defined using the circumferentially averaged turbulence intensity (taken directly from the turbulent kinetic energy) and the circumferentially averaged integral length scale.

It is important to point out that mapping the actual vane geometry onto a required flat plate geometry at each radial location is not unique. One must choose a stagger angle at which to set the flat plate cascade representation. In Figure 18 the effect of changing the stagger selection on the broadband noise prediction for the SDT 54-vane baseline case at the approach condition is shown. Three methods for selecting the stagger angle have been used. First the stagger angle is obtained by using a weighted average of the leading and trailing edge staggers of the real vanes: a) 10% leading edge stagger, 90% trailing edge stagger; b) 90% leading edge stagger, 10% trailing edge stagger. Finally, the stagger is selected to match the stagger at the midchord: c) 100% midchord stagger. The results shown in Figure 18 correspond to the downstream interaction noise spectrum. An additional data set is included on the plot. The x's represent previously reported computational results for the broadband sound

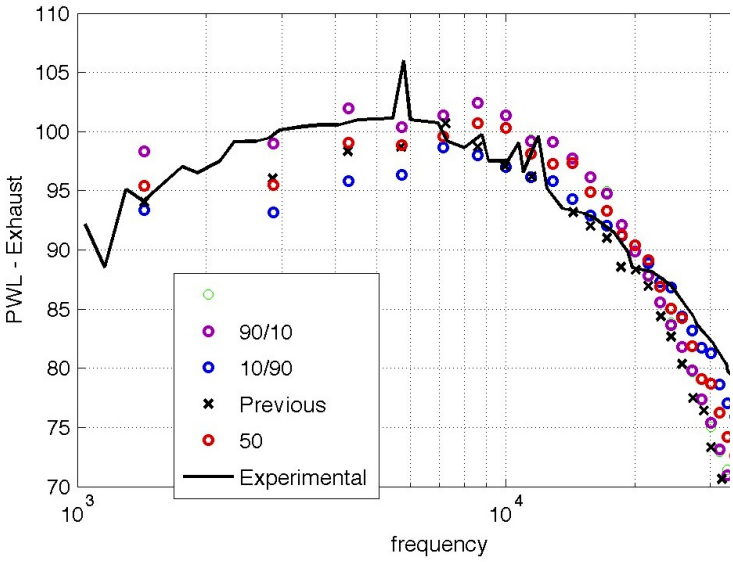

FIGURE 18. Effect of stagger angle selection on broadband comp tation.

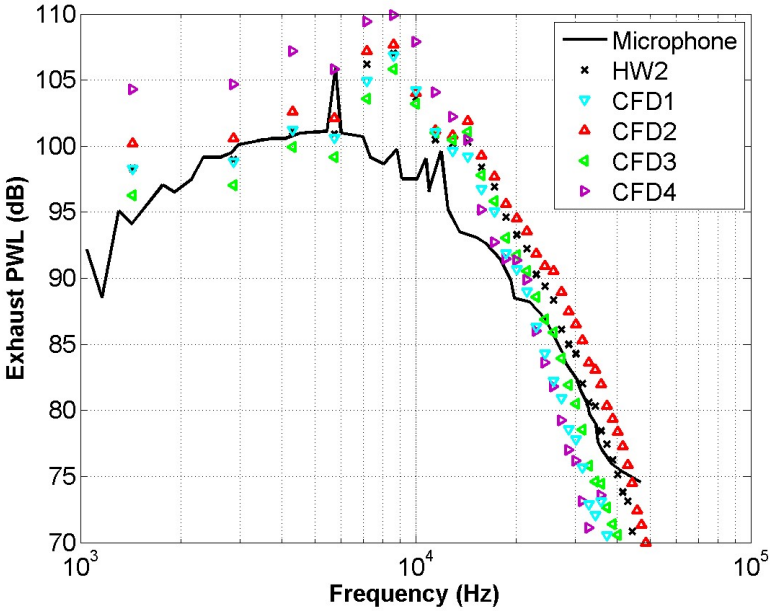

FIGURE 19. Exhaust broadband noise prediction from RSI based on input derived from four different CFD simulations and experimental data.

associated with this SDT case [14]. The experimental spectrum includes the tones at 2, 3 and 4 BPF that are not computed as part of the broadband prediction. As one changes the stagger angle selection from the trailing edge to the leading edge, the predicted noise increases at the lower frequencies (< 20000Hz) and decreases at higher frequencies.

Because the trend with stagger is fixed and accountable, one can use this method with any of the 3 stagger angle selection methods to compare the impact of the differing CFD solutions on the broadband calculation. Here the stagger angle computed as 90% leading edge and 10% trailing edge stagger is used for each simulation. Figure 19 compares the predicted acoustic power spectrum based on the different CFD predictions of the k distribution in the passage, the circumferentially averaged value of k and the circumferentially averaged value of the integral length scale.

Two further computations were performed in order to specify which turbulence parameter has a greater effect on the broadband prediction. First, all of the input values except the integral length scale were set to be the values obtained from the experimental data. This replaces the predicted turbulent kinetic energy by the experimental value. The results are shown in Figure 20. This change in input does little to affect the results. It raises the PWL almost uniformly for all of the simulations.

Second, the CFD determined value of the turbulent kinetic energy is used but the experimental length scale is specified in all of the input files. Figure 21 has the results from this set of computations. This replacement collapses the data to basically two curves. The difference between the two curves is generated by the difference in the background level of the turbulence. These two input substitutions indicate that the integral length scale and the background turbulence intensity values are the more important RSI input parameters. These results highlight a hurdle that must be overcome in order to create a fully computational method for predicting the broadband noise.

6 Summary and Conclusions

The Source Diagnostic Test baseline vane case at the approach condition was used as a platform for studying the effect of calculated turbulence parameters on a broadband fan noise calculation. A comparison is shown between predicted turbulence parameters in the gap that extends from the fan to the FEGV from four RANS simulations and parameters obtained from the experimental data. The experimental values were obtained utilizing structure functions and various scaling laws. The turbulent kinetic energy and mean dissipation were taken directly from the CFD simulations which utilized two-equation turbulence models. The k value compared well with experiment and the trend in ε when circumferentially averaged also agreed with experiment. However, the magnitude of ε was quite high compared to the experimental value. Two methods for obtaining the integral length scale were used in conjunction with the experimental data. The method based on structure functions was used to obtain a passagewise distribution of the integral length scale as well as a circumferentially averaged value. The averaged integral

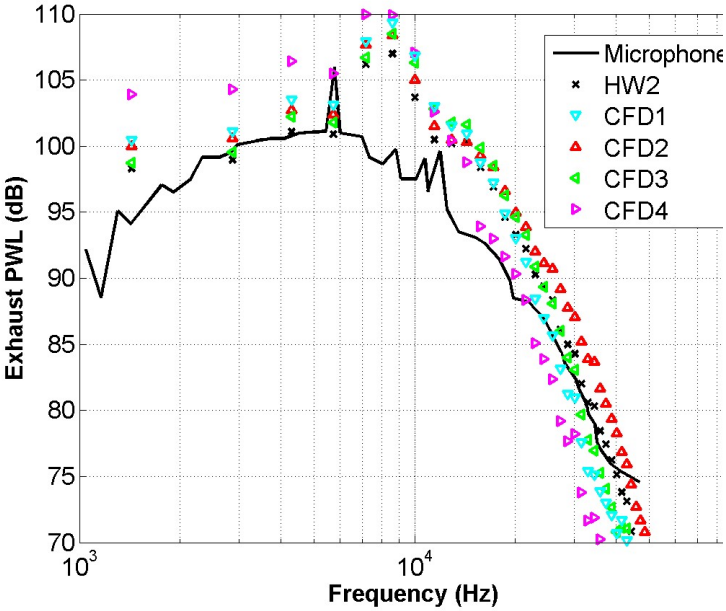

FIGURE 20. Experimental turbulent kinetic energy, CFD determined integral length scale.

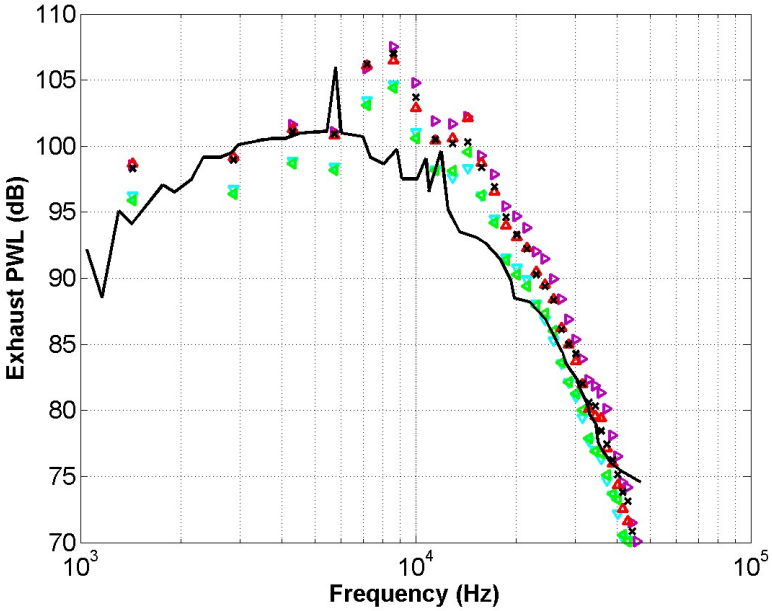

FIGURE 21. Experimental integral length scale, CFD determined turbulent kinetic energy.

length scale was also computed using the autocorrelation. These two methods lead to different radial distributions of the integral length scale and disagree by a factor of two near the hub. An estimate of the integral length scale was also obtained from the simulations. The circumferentially averaged values of the predicted integral length scale compared reasonably well with the values from the experiment.

The RSI code was used to predict the broadband noise downstream of the vane. The turbulent kinetic energy and integral length scale upstream of the vane are critical input values to RSI along with the mean flow and geometry specifications. The prediction from RSI is shown to vary consistently with the selection of stagger angle definition. Given a specific stagger angle definition, the effect of changing the input based on the different CFD results was shown. Modification of the input files so that different parameters were replaced by the experimental values allowed for separation of some effects. It was shown that differences in the specification of the integral length scale and in the background level of the turbulence intensity had the largest affect on the broadband noise prediction. In order to improve the accuracy of the fully computational hybrid broadband noise prediction method, a more reliable method for determining the length scale and accounting for (and not limiting) the background turbulence is needed.

Further investigation is planned in order to determine if accurate broadband noise trends can be achieved using the current computational hybrid approach. Similar broadband noise predictions will be made for the higher wheel speeds which were part of the SDT. The difference between the CFD generated input for these cases will be shown however no hot-wire data are available for comparison. Again, the importance of the various RSI input parameters will be considered.

ACKNOWLEDGMENT

The authors would like to thank Drs. A, Sharma, B. Morin, and E. Envia for providing CFD simulation results. Dr. Envia also supplied the relevant experimental test specifications.

The authors would also like to recognize the following people (from NASA Glenn unless otherwise noted): CFD code development: Daniel L. Tweedt, (AP Solution Inc.), Timothy A. Beach, Amir A. Shabbir, Mark A. Celestina, Scott A. Thorp, Richard A. Mulac, and John J. Adamczyk (retired); SDT hotwire data: Gary G. Podboy.

Finally, the authors acknowledge partial financial support through the Ohio Aerospace Institute in the form of the Aeroacoustics Research Consortium grant number R-700-400301-40125. Additional thanks to the AARC members for their constructive input.

REFERENCES

[1] Envia, E., Tweedt, D., Woodward, R. P., Elliot, D. M., Fite, E. B., Hughes, C. E., Podboy, G. G., and Sutliff, D. L.,

2008. “Assessment of current fan noise prediction capability”. *AIAA Paper No.2008-2991*. 14th AIAA/CEAS Aeroacoustics Conference.

[2] Podboy, G. G., Krupar, M. J., Helland, S. M., and Hughes, C., 2003. Steady and unsteady flow field measurements within a nasa 22-inch fan model. Tech. Rep. TM-2003-212329, NASA.

[3] Maunus, J., Grace, S. M., and Sondak, D. L., 2010. “Effect of rotor wake structure on fan interaction noise”. *AIAA Paper No. AIAA 2010-3746*. 16th AIAA/CEAS Aeroacoustics Conference.

[4] Maunus, J., Grace, S. M., and Sondak, D. L., 2010. “Effect of rotor wake structure on fan interaction noise”. *AIAA Journal,* ***Under Review***.

[5] Kolmogorov, A., 1991. “Dissipation of energy in the locally isotropic turbulence”. In Preceedings: Mathematical and Physical Sciences, Vol. 434-1890, pp. 15–17.

[6] Monin, A. S., and Yaglom, A., 1971. *Statistical Fluid Mechanics: Mechanics of Turbulence Volume II*. MIT Press, Cambridge, MA.

[7] Oberlack, M., 1997. “Non-isotropic dissipation in non-homogeneous turbulence”. *Journal of Fluid Mechanics,* ***350***, pp. 351–374.

[8] Camp, T., and Shin, H.-W., January 1995. “Turbulence intensity and length scale measurements in multistage compressors”. *Journal of Turbomachinery,* ***117***, pp. 38–46.

[9] Axelsson, L.-U., and George, W., 2008. “Spectral analysis of the flow in an intermediate turbine duct”. *ASME,* ***6***, pp. 1419–1426. ASME Turbo Expo 2008: Power for Land, Sea, and Air (GT2008).

[10] Frisch, U., 1995. *Turbulence: The Legacy of A.N. Kolmogorov*. Cambridge University Press, Cambridge, UK.

[11] Donzis, D. A., Sreenivasan, K. R., and Yeung, P. K., 2005. “Scalar dissipation rate and dissipative anomaly in isotropic turbulence”. *Journal of Fluid Mechanics,* ***532***, pp. 199–216.

[12] Doering, C. R., and Foias, C., 2002. “Energy dissipation in body-forced turbulence”. *Journal of Fluid Mechanics,* ***467***, pp. 289–306.

[13] Seoud, R., and Vassilicos, J., 2007. “Dissipation and decay of fractal-generated turbulence”. *Physics of Fluids,* ***19***, pp. 105108–105108–11.

[14] Nallasamy, M., and Envia, E., 2005. “Computation of rotor wake turbulence noise”. *Journal of Sound and Vibration,* ***282***, pp. 649–678.

[15] Ventres, C., Theobald, M. A., and Mark, W. D., 1982. Turbofan noise generation volume 1: Analysis. Tech. Rep. CR-167952, NASA, July.

[16] Woodward, R. P., 2002. “Fan noise source diagnostic test-farfield acoustic results”. *AIAA Paper No. 2002-2427*. 8th AIAA/CEAS Aeroacoustics Conference.